Stick-slip dynamics of cell adhesion triggers spontaneous symmetry breaking and directional migration of mesenchymal cells on one-dimensional lines

K. Hennig, I. Wang, P. Moreau, L. Valon, S. Debeco, M. Coppey, Y. A Miroshnikova, C. Albigès-Rizo, Cyril Favard, R. Voituriez, et al.

CELL BIOLOGY

Stick-slip dynamics of cell adhesion triggers spontaneous symmetry breaking and directional migration of mesenchymal cells on one-dimensional lines

K. Hennig[1], I. Wang[1], P. Moreau[1], L. Valon[2], S. DeBeco[3], M. Coppey[3], Y. A. Miroshnikova[4], C. Albiges-Rizo[4], C. Favard[5], R. Voituriez[6]*, M. Balland[1]*

Directional cell motility relies on the ability of single cells to establish a front-rear polarity and can occur in the absence of external cues. The initiation of migration has often been attributed to the spontaneous polarization of cytoskeleton components, while the spatiotemporal evolution of cell-substrate interaction forces has yet to be resolved. Here, we establish a one-dimensional microfabricated migration assay that mimics the complex in vivo fibrillar environment while being compatible with high-resolution force measurements, quantitative microscopy, and optogenetics. Quantification of morphometric and mechanical parameters of NIH-3T3 fibroblasts and RPE1 epithelial cells reveals a generic stick-slip behavior initiated by contractility-dependent stochastic detachment of adhesive contacts at one side of the cell, which is sufficient to trigger cell motility in 1D in the absence of pre-established polarity. A theoretical model validates the crucial role of adhesion dynamics, proposing that front-rear polarity can emerge independently of a complex self-polarizing system.

INTRODUCTION

Directional motility is a plastic process (*1*) that is the fundamental basis of key biological processes in eukaryotes, such as embryonic morphogenesis, leukocyte trafficking in immune surveillance, and tissue regeneration and repair (*2*, *3*, *4*). Furthermore, aberrations in signaling pathways regulating cell migration contribute to tumor invasion (*5*) and metastasis (*6*). Over the past decades, two main modes of migration have been identified: adhesion-dependent mesenchymal (*7*) and adhesion-independent amoeboid migration (*8*). These migration modes differ in the way forces are generated and transduced within the cell. However, the breaking of cell symmetry is a fundamental process at the basis of any migration event (*9*, *10*).

In the absence of external polarity cues, several mechanisms of spontaneous symmetry breaking have been proposed and are based on polarization of cytoskeleton components (*11*). For instance, gradients or patterns of morphogens can arise because of specific reaction-diffusion patterns within the cell, leading to its polarization (*12*). More recently, several mechanisms of spontaneous symmetry breaking of the actomyosin system itself have been proposed, on the basis of either actin polymerization (*13*, *14*) or actomyosin contractility (*15*, *16*, *17*). However, relating these symmetry breaking events of various components of the cellular cytoskeleton to both cell-substrate forces and cell locomotion remains largely unexplored.

In the specific case of mesenchymal migration, the spatiotemporal sequence of mechanical symmetry breaking remains controversial. Different models are distinguished by the temporal order in which distinct cytoskeleton forces are activated to trigger directional movement (*18*). Most studies emphasize force generation due to actin polymerization in the cell front as a first step to initiate migration (*3*, *19*, *20*). On the contrary, actomyosin II–mediated contractility within the cell rear has been identified as a first step to break cell symmetry in keratocytes (*21*). Thus, determining the spatiotemporal dynamics of cellular forces and morphological events at the initiation of migration is still an open and major question in biology.

To address this question, we developed a single-cell one-dimensional (1D) migration assay based on real-time force imaging, quantitative microscopy, and soft micropatterning to dynamically quantify in parallel mechanical and morphological parameters during spontaneous symmetry breaking. We found that mesenchymal cells confined to thin adhesive one-dimensional (1D) lines had a characteristic spatial force pattern, from which migratory and multipolar force parameters could be extracted in a straightforward and simplified manner. Our analysis demonstrates the critical role of force-mediated adhesion detachment in the rear of the cell. In particular, we show that migration can occur in the absence of a preestablished cytoskeleton polarity. A theoretical model based on the experimentally observed stick-slip motion shows that these patterns are controlled by coupled dynamics of the actomyosin-generated contractility and cell-substrate adhesion dynamics. We show that this coupling induces correlation between cell speed and cell length, which we could observe by analyzing single-cell trajectories of multiple cell lines, confirming the robustness of the proposed stick-slip behavior.

RESULTS AND DISCUSSION

Quantitative migration assay to probe the dynamic force modulations during spontaneous symmetry breaking in 1D

To quantitatively investigate the dynamics of spontaneous symmetry breaking events in cells at the level of both morphological parameters

[1]Laboratoire Interdisciplinaire de Physique, Grenoble Alpes University, Saint Martin d'Heres, France. [2]Institut Pasteur, Department of Developmental and Stem Cell Biology, 25 rue du Dr. Roux, 75015 Paris, France. [3]Laboratoire Physico-Chimie, Institut Curie, Centre National de la Recherche Scientifique UMR168, Paris, France. [4]DYSAD, Institut for Advanced Biosciences, Centre de Recherche UGA/Inserm U 1209/CNRS UMR 5309, La Tronche, France. [5]Membrane Domains and Viral Assembly, IRIM, UMR9004 CNRS/Université de Montpellier, 1919, route de Mende, 34293 Montpellier Cedex, France. [6]Laboratoire Jean Perrin and Laboratoire de Physique Théorique de la Matière Condensée, Sorbonne Université, Tour 13-12, 5eme etage, 4 place Jussieu, 75252 Paris Cedex 05, France.
*Corresponding author. Email: martial.balland@univ-grenoble-alpes.fr (M.B.); voiturie@lptmc.jussieu.fr (R.V.)

and distribution of interaction forces with the environment, we developed a 1D migration assay (Fig. 1A) that combined time-resolved traction force microscopy (TFM) (*22*, *23*, *24*) and soft micropatterning (*25*).

Using this bottom-up approach, we followed single epithelial cells [hTERT (human telomerase reverse transcriptase)–immortalized retinal pigment epithelial cell line (RPE1)] during the initiation of spontaneous migration and extracted morphometric and mechanical parameters. As expected (*26*, *27*), RPE1 cells plated on patterned 40-kPa polyacrylamide hydrogels adhered to 1D fibronectin lines (2- or 5-μm width) within 1 to 2 hours. The cells displayed elongated shapes with long actin fibers oriented parallel to the micropattern and cell axis (Fig. 1B).

In the absence of any external cue, we observed a biphasic motile behavior: symmetric elongation of a static cell (spreading phase) before spontaneously initiated directional movement (migration phase; Fig. 1C). In parallel, tangential stress measurements revealed defined stress compartments at both cell edges due to contractile forces oriented toward the center of the cells (Fig. 1D). Hence, cells behaved as force dipoles, as described previously (*14*, *28*, *29*, *30*). During the spreading phase, both cell elongation dynamics and force distribution patterns were fully symmetric with respect to the cell center of mass. At the onset of motility, morphological polarization and simultaneous asymmetrical redistribution of forces occurred, characterized by a single defined local stress compartment at the cell front and a substantially widened stress distribution with lower traction stress at the rear (Fig. 2A). This was accompanied by rapid retraction of the cell rear (Fig. 1D).

Current models emphasize the formation of a distinct cell front as the first event when cell migration is initiated (*10*, *31*). In contrast, we observed that cell spreading was qualitatively symmetric on both sides and that symmetry breaking occurred with the sudden retraction of the rear. This led us to hypothesize that contractility builds up in a nonpolarized cell, resulting in a local stress increase at both extremities until adhesions in the prospective rear detach.

Single migrating cells display a stochastic stick-slip behavior due to the coupled dynamics of contractility and adhesions

To challenge the hypothesis that symmetry breaking does not require preestablished rear-front polarity as previously thought (*32*, *21*), we quantified the coordination between mechanical polarization and morphological events. To first confirm the qualitative observation of anisotropic redistribution of traction forces, we adapted multipolar analyses, classically used in the field of microswimmers (*33*), to our 1D conditions to quantify the asymmetry of the force distribution. We first projected the stress profile along the micropattern axis to obtain a 1D stress profile, a mechanical footprint of the cell. From that, we computed the variance of positive- and negative-directed traction stress profiles (D_+, D_-), which quantified the spatial distribution of each stress compartment at opposite poles of the cell. The normalized ratio, $(D_+ - D_-)/(D_+ + D_-)$ (analogous to the normalized stress quadrupole), quantifies the symmetry of the spatial stress distribution and will be referred to as force asymmetry parameter (Fig. 2A).

Nonmigrating cells exhibited a force asymmetry parameter fluctuating around zero, indicating a nonpolarized static phase (Fig. 2A). Consistently, fluctuations in the actin profiles were also observed in static phases (fig. S1). No significant polarization of actin distribution was observed before migration initiation. Nevertheless, upon initiation of each migration step, the force asymmetry parameter displayed a sharp transient peak. This sudden increase corresponded to a widening of the spatial stress distribution in the rear of the cell while the stress pattern at the cell front remained localized to the cell edge. This asymmetry subsequently relaxed, leading to another static phase. Several iterations of such phases were typically observed. Consistently, we found larger values in the amplitude of the asymmetry parameter in moving phases in comparison to the static ones for multiple analyzed cells. Thus, initiation of migration is characterized by a sharp increase of the force asymmetry parameter and can occur in the absence of prior polarization of the actin cytoskeleton.

We subsequently hypothesized that stress builds up and fluctuates during the spreading phase until one end randomly detaches, producing a cell rear. This hypothesis was supported by the evolution of the total traction force, a measure of the strength of the mechanical interaction of the cell with the substrate, quantified via TFM. We observed that, in static phases, cell spreading was associated with an increase of the total traction force. Upon the initiation of migration, the force level dropped by approximately 50% (fig. S2). Notably, this decrease in mechanical interaction was directly correlated with a shortening in cell length due to the sudden retraction of the rear (Fig. 2B and fig. S3). To confirm the role of adhesion detachment, we fluorescently labeled cell-substrate anchor points using vinculin–enhanced green fluorescent protein (vin-eGFP) to follow the time evolution of adhesion patches during migration. As previously described (*34*), adhesion sites at the front of the cell were continuously contacting the substrate, while adhesion sites at the rear followed two distinct phases: attachment (cluster growth) and switching abruptly to detachment (disassembly and sliding of smaller adhesion patches; Fig. 2C). Cell morphology and its polarity features showed similar behavior as after the initial symmetric spreading phase, abrupt retraction of the rear triggered subsequent nuclear translocation. Furthermore, throughout the migration cycle, the trailing edge displayed two distinct phases of motion, while the front continuously moved forward (Fig. 2C). This destabilization of the trailing edge demonstrated the critical role of adhesion detachment in the back of the cell. The observed discontinuous migration is similar to what is known in physics as a stick-slip mechanism (Fig. 2D). During the initial spreading phase, cells elongated symmetrically while increasing their contractile stress (stick). Upon reaching a level of stress that adhesion complexes could no longer sustain, adhesions on one cell edge stochastically detached from the substrate. This led to cell shortening due to retraction of the rear and a decrease in cell-substrate interaction (slip). Recovery of the initial cell length and contractility level occurred during the subsequent stick phase. As a consequence of this stick-slip migration, the propensity of cells to enter migratory phases appeared to crucially depend on (i) contractility and (ii) adhesion properties.

To substantiate this observed stochastic stick-slip behavior, we devised a physical model based on minimal ingredients (see the Supplementary Materials for detailed description). The actin cytoskeleton was described as an active, homogeneous 1D viscoelastic gel (*35*). We assumed that the cell's cytoskeleton was fully unpolarized and that the cell body could be mechanically characterized by an effective stiffness k. This elastic behavior encompasses active (i.e., because of motor activity) and passive contributions of both cytoskeleton and membrane. Adhesion sites were described in the framework of the active gel theory as localized regions at both cell extremities carrying outward pointing actin polarity $\boldsymbol{p}$ and subjected to an active force $\boldsymbol{F_a}=\chi\,\boldsymbol{p}$, where χ is a phenomenological coupling constant, which induced cell expansion. The key ingredient of the model

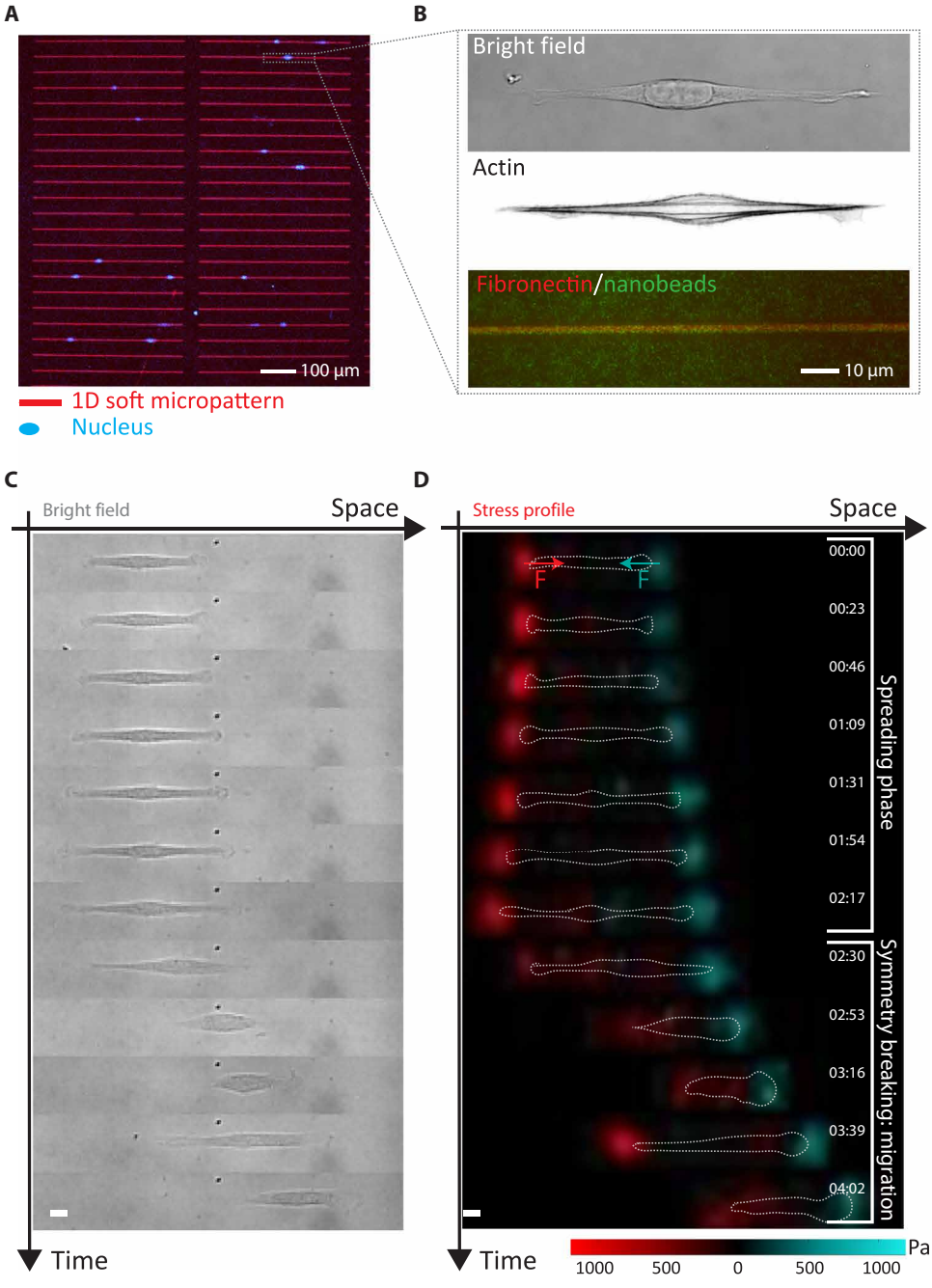

Fig. 1. 1D single-cell migration assay based on soft micropatterning and TFM mimics complex 3D fibrillar in vivo migration. (**A**) Polyacrylamide gel (40 kPa) with RPE1 cells (blue, nucleus staining) on top of 2-µm micropatterned fibronectin lines (red). (**B**) Bright-field, actin cytoskeleton, and bead imaging of RPE1 on a 2-µm line allowed extracting morphometric and mechanical parameters simultaneously. (**C**) Time sequence of RPE1 cell migrating on fibronectin lines and (**D**) its associated stress profile extracted via TFM (dotted white line, cell outline; color-coded stress profile depending on the direction of applied traction forces $\vec{F}$: red in and cyan against the direction of migration. Scale bars, 10 µm).

relies on the dynamics of adhesion sites, which was written phenomenologically as $\dot{p} = g(v_p) - \lambda p$. Here, λ models the rate of actin turnover, and g the dynamics of adhesion sites assembly that depends on the local velocity $v_p = v \cdot u_p$ over the substrate. g is a priori very asymmetric (Fig. 2E). This accounts for the fact that adhesion assembly is drastically reduced upon edge retraction and mildly affected by edge expansion. The analysis of the model revealed that the actin turnover rate critically controls the dynamics. In particular, at a slow turnover rate (as defined in the Supplementary Materials), the system was found to display a stochastic stick-slip behavior, (which notably differs from classical stick-slip behaviors characterized by deterministic oscillations). Cells were predicted to slowly expand and reach the fixed point of the dynamics where any fluctuation leading to infinitesimal retraction is unstable: One end of the cell

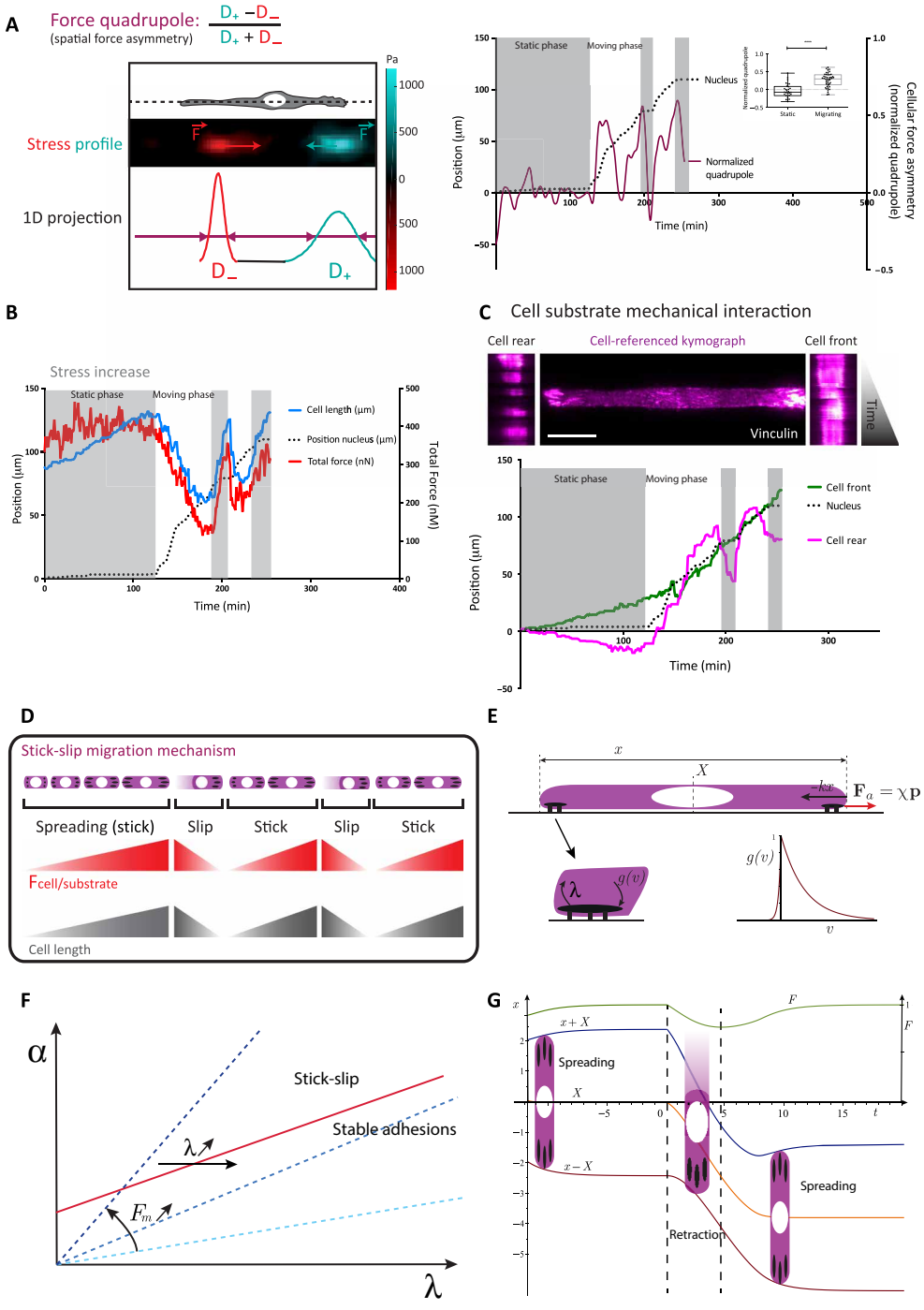

Fig. 2. RPE1 cells exhibit intermittent migration following a stick-slip motion. (**A**) Scheme of the force asymmetry analysis: The normalized quadrupole was extracted from the 1D projection of the stress profile of an adherent cell (color-coded stress map and 1D profile depending on the direction of applied traction forces $\vec{F}$ exerted: red in and cyan against the direction of migration). Dynamic measurements revealed a symmetric spatial force profile during static spreading and an asymmetric distribution during migration phases. Inset: average force asymmetry during static and mobile phases of several cells ($n = 10$). ****$P < 0.0001$ (unpaired, two-tailed t test). (**B**) Cell length and total force correlation: increase during spreading phase and decrease during migration. (**C**) Referenced kymograph of RPE1 cells stably expressing vinculin-eGFP showing a continuous attachment of the front, while adhesions in the rear detached and reattached during one migration cycle (scale bar, 10 µm). Tracking the front, rear, and nucleus position over time could further represent this destabilization of the rear. (**D**) Deduced scheme of the proposed stick-slip migration mechanism: During nonmotile spreading (stick), the cell builds up a high traction force that eventually will overcome adhesion strength in the perspective rear of the cell. Upon the retraction of the rear, the cell shortens and lowers its mechanical interaction with the substrate to initiate migration (slip). (**E**) Schematic of the model and parameters as defined in the text. (**F**) Phase diagram of dynamic behaviors predicted by the model, as a function of the actin turnover rate λ and phenomenological parameter α (arbitrary units). Dashed lines show different values of the maximal contractile force $F_{max} = \frac{\chi\alpha}{\lambda}$. (**G**) Example of stick-slip dynamics predicted by the model. Dynamical eqs. S2 and S3 are solved numerically with $vm = 0.5$, $\boldsymbol{v_p} = 0.5$, $\lambda = 1$, $\boldsymbol{\mu} = 1$, $\alpha = 1$ (arbitrary units). Blue, orange, and brown line show rear, nucleus, and front position over time, respectively. Green line depicts the relative traction force level F.

therefore retracts before spreading symmetrically again. Last, the model successfully predicts that dynamics are critically controlled by the adhesion turnover rate λ and the maximal contractile force, as summarized in the phase diagram of Fig. 2F, and reproduces the observed stochastic stick-slip dynamics (Fig. 2G).

Of note, the 1D model that we present here is based on the dynamics of cell edges that extend in opposite directions during spreading. A simple generalization of the model from 1D to higher dimensions would be to consider *N*-competing protrusions (instead of two in the 1D setting) described by the dynamics introduced above while preserving global force balance. In this case, a similar stochastic stick-slip scenario (force buildup until adhesions rapture) can be expected in 2D or 3D environments; this is left for further works.

Local RhoA optogenetic stimulation triggered rear formation and mimicked the initiation of migration

To challenge the proposed stochastic stick-slip mechanism, we used optogenetics to disrupt its predicted spatiotemporal sequence. We used NIH-3T3 cells stably expressing a Cry2-CIBN (N-terminal domain of cryptochrome-interacting basic-helix-loop-helix) optogenetic probe to dynamically control the localization of ArhGEF11, an upstream regulator of the master regulator of cell rear retraction, RhoA [from now on referred to as optoGEF_RhoA; (*36*)]. Upon stimulation with blue light, optoGEF_RhoA dimerizes with the CAAX-anchored protein CIBN, leading to its immediate translocation from the cytoplasm to the membrane where it activates RhoA, triggering asymmetric recruitment of actin and subsequent cell migration away from the photoactivation spot. The initiated movement was characterized by a distinct front-rear polarity that was maintained throughout the whole stimulation cycle. By switching the side of stimulation, actin polarity and direction of movement were inverted (Fig. 3A).

This optogenetic approach combined with quantitative force measurements revealed a RhoA-mediated instantaneous and local increase of traction forces in the zone of activation. This transient and spatially confined force increase was followed by a global decrease of the mechanical interaction of the moving cell with its substrate, as seen on the total traction force (Fig. 3B). This drop was similar to the one observed during spontaneous migration (Fig. 2C), which was attributed to adhesion detachment at the cell rear. To confirm that the same process was at play here, we imaged adhesions by transiently transfecting optogenetic cells with vin-iRFP (infrared fluorescent protein). Upon light-induced RhoA activation, we observed first reinforcement, then detachment and sliding of adhesions (Fig. 3C). As actomyosin contractility was stimulated, adhesions were submitted to an increasing level of stress that first led to vinculin recruitment (positive feedback) (*37*) but ultimately caused adhesions to dissociate. Hence, local stimulation artificially created the cell rear, triggering the first step of cell translocation (adhesion detachment) as in the case of spontaneous migration.

Tuning adhesion/force balance switched migratory behavior of NIH-3T3 and RPE1

A key prediction of the stick-slip model is that spontaneous symmetry breaking strongly depends on contractility and adhesiveness. To challenge this prediction and to further investigate the stick-slip migration mechanism illustrated in Fig. 2, we systematically analyzed the main parameters of our theoretical model (cell length, adhesion size, and total traction forces) and correlated them with the migratory parameters of single cells of two distinct cell types exhibiting different motile behaviors. The instantaneous speed of the cell centroid was used as a parameter to represent the migration capacity of single cells. To test the broader applicability of the model, fast-migrating RPE1 (*38*) cells were compared to fibroblast cells (NIH-3T3) that exhibit slow mesenchymal migration (*39*).

RPE1 cells exhibited a higher speed compared to NIH-3T3 that mostly remained in a static spreading phase with less frequent retraction phases. Comparing cell morphology and traction force level of both cell types, we observed that NIH-3T3 cells exhibited a longer spreading length associated with a larger mechanical interaction of the cells with their microenvironment (Fig. 4A). This result may appear counterintuitive as larger traction forces should facilitate detachment of adhesions and thus cellular movement. However, in the classical catch-bond model, an increase of force would also induce a stabilization and reinforcement of adhesion sites (*40*). Consistent with this, NIH-3T3 cells had larger adhesion patches compared to RPE1 cells.

To analyze adhesion strength in more detail, we quantified adhesion dynamics in both cell types. First, total internal reflection fluorescence microscopy (TIRFm) of vin-eGFP adhesions revealed faster adhesion turnover in RPE1 cells compared to NIH-3T3 fibroblasts (movie S1). To further quantify the difference in adhesion dynamics between both cell types, we performed fluorescence recovery after photobleaching (FRAP) experiments on adhesive patches localized at edges of nonmotile cells. To do so, we specifically chose cells that had well-defined symmetric morphologies, indicating that these cells were unlikely to migrate (stick phase). We were thus able to assure measurements independent of any potential intracellular front-rear polarity effects, which might arise during slip phases, by performing FRAP experiments on random sides for a high number of nonpolarized static cells. These FRAP experiments revealed two time components: a fast one that was related to the diffusion of vinculin molecules within the cytosol and a slow one corresponding to the residence time of immobilized vinculin within the adhesion sites (Fig. 4B). The measured slow and fast component ratios revealed that RPE1 cells displayed a lower fraction of bound vinculin compared to NIH-3T3. Since vinculin binding promotes adhesion stability, our data indicated that RPE1 cells exhibited more labile adhesions, while NIH-3T3 adhesions were expected to sustain higher tension without breaking. These findings are in agreement with the stick-slip model since faster RPE1 cells would undergo fast spreading/retraction cycles (large λ), while less motile NIH-3T3 relaxed more slowly to the unstable fixed point (small λ). Therefore, the migratory behavior of these two cell types could be explained, in the framework of our stick-slip model, by cells having different levels of adhesiveness and contractility.

To further confirm the validity of this model, we used pharmacological treatments to perturb the balance between adhesiveness and contractility. We used a low dose of blebbistatin (3 μM) to decrease contractility (*41*) in NIH-3T3 fibroblasts and 1 μM pF573,228 to stabilize adhesions (*42*) in RPE1 cells. As both parameters (contractility and adhesion strength) are bidirectionally coupled through positive feedback loops (*40*, *43*, *44*), one could not be modulated without affecting the other. Blebbistatin-treated NIH-3T3 cells were more readily able to initiate migration, as shown by the increase of their migration speed (Fig. 4C). They exhibited a decrease of total traction force as expected, but also a shortening of the average cell

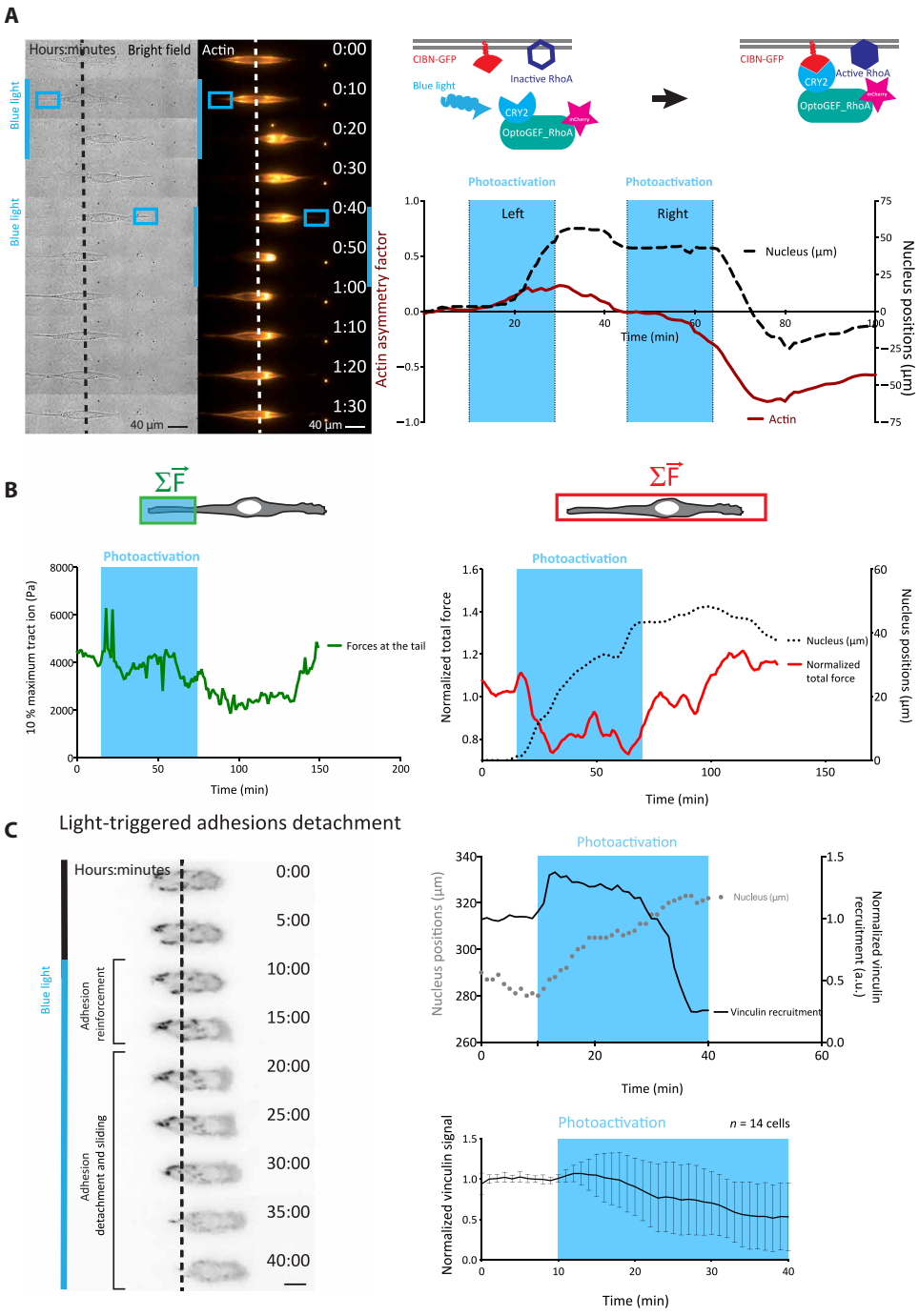

Fig. 3. RhoA optogenetic control of cellular force symmetry breaking. (**A**) Schematic representation of light-induced Cry2-CIBN dimerization and local RhoA activation due to its close proximity to its upstream regulator optoGEF_RhoA. Bright-field and actin imaging and quantification showed the light-induced migration away from the photoactivation area (blue square), which is characterized by a transient front-rear polarity and actin asymmetry (dashed line, nucleus position at *t*0). (**B**) Local and global force response of the light-induced rear and of the whole cell, respectively, showed a transient local contractility increase at the perspective rear followed by a global decrease of the mechanical cell-substrate interaction. (**C**) Cells stably expressing vinculin-iRFP revealed local adhesion reinforcement within the photostimulated area followed by a subsequent adhesion detachment. Dashed line indicates nucleus position at *t*0. Scale bar, 10 µm. a.u., arbitrary units.

length, which suggested that these cells can more easily detach their adhesions. The size of adhesion patches decreased significantly upon blebbistatin treatment (Fig. 4C). Hence, by inhibiting contractility, cell adhesiveness was lowered, which facilitated the rear detachment and led to cell shortening and increased motility. In agreement with the stick-slip model, low maximal contractile force corresponded to low cell/substrate interactions, giving rise to reduced cell spreading and therefore smaller cell length and potentially larger speeds (provided that the cytoskeleton is polarized).

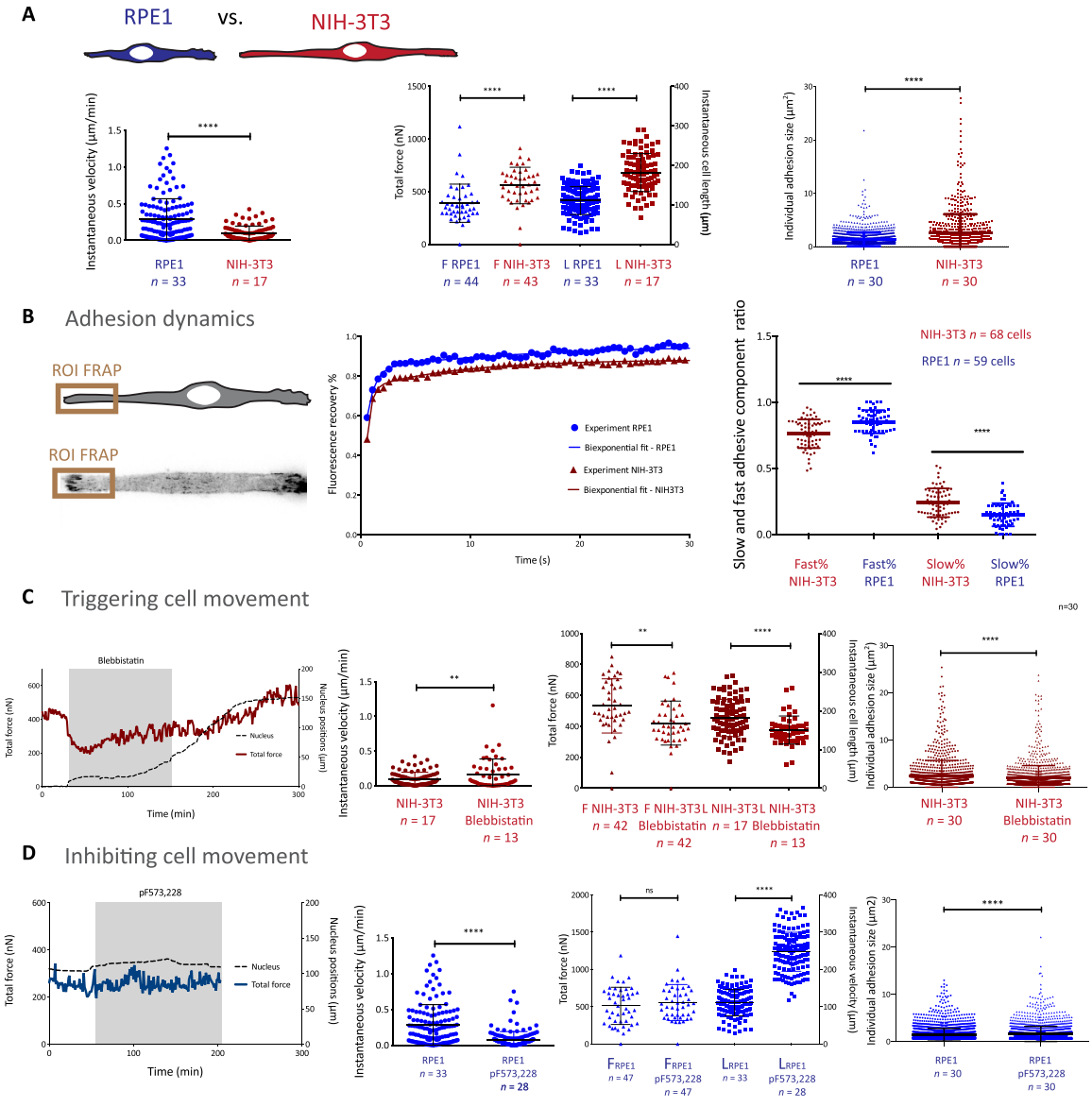

Fig. 4. Adhesiveness and contractility control the migratory behavior of NIH-3T3 and RPE1 cells. (**A**) Comparison of instantaneous migration speed, total force, cell length, and individual adhesion size of RPE1 and NIH-3T3 cells. (**B**) FRAP experiments of adhesions located at one cell edge were modeled with a biexponential fit to extract a fast and slow component representing mobile vinculin within the cytoplasm and slow vinculin bound to adhesions. ROI, region of interest. (**C** and **D**) Altering the migratory behavior of RPE1 and NIH-3T3 using 1 μM pF573,228 to inhibit and 3 μM blebbistatin to trigger migration, respectively. Shown are measured parameters relevant for stick-slip migration: average migration speed, total force, cell length, and individual adhesion size. Statistical significance tested with unpaired two-tailed *t* test. Scatter plots with means and SD. Box plots from minimum and maximum values with the means and SD. Number *n* of analyzed cells per condition indicated on the respective graph figures. ****$P<0.0001$; **$P<0.01$; ns, not significant.

On the contrary, stabilizing focal adhesions on RPE1 cells decreased their velocity. It also induced a lengthening of the cells and larger adhesion patches (Fig. 4D) as predicted by our model: Diminishing the turnover rate λ induces a marked stick-slip behavior, with long spreading phases, and therefore large cell length, and slow speed. The dependence of the stick-slip behavior on the turnover rate and contractility results in inverse correlation between average cell length and migration velocity (Fig. 5A), which was consistently observed in both NIH-3T3 and RPE1 cells. More elongated cells, such as NIH-3T3, were associated with stronger adhesions, as they could spread more without detaching, and hence a lower velocity. When this detachment occurred at an early stage of spreading, corresponding to low stress levels, cells were shorter and exhibited higher migration speeds, as in the case of RPE1.

Stochastic stick-slip behavior induces a robust coupling between cell length and cell speed

Last, we asked whether the stick-slip paradigm would operate also in the presence of additional polarization mechanisms. We used deposited data of single-cell trajectories of various cell types on patterned adhesive 1D lines [First World Cell Race (*39*)]. For each cell line, both instantaneous cell speed and cell length were extracted

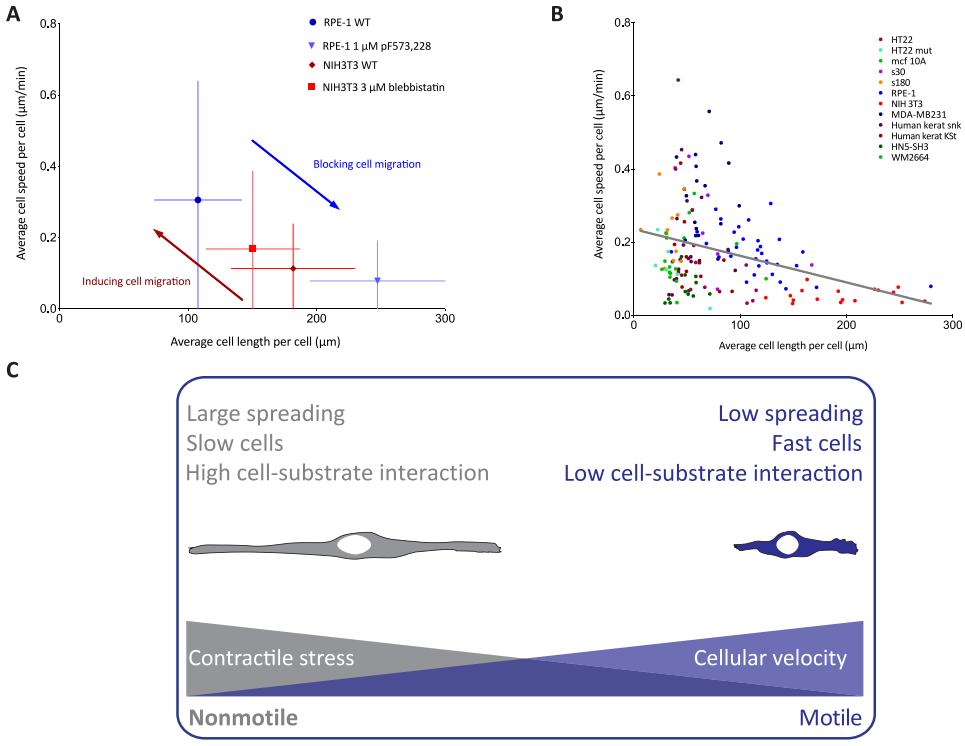

Fig. 5. The inverse relation between cell length and speed. (**A**) Experimentally deduced phase diagram using a pharmacological approach to alter the migratory behavior of RPE1 and NIH-3T3 cell (error bars show the SD from the mean). (**B**) Length-speed relation validated by analyzing several cell types coming from the cell race data (one color used per cell type; gray line, linear fit of all data points). (**C**) Summary showing how cell contractility, and therefore adhesiveness and cell length, control cellular migration.

and correlated with each other (Fig. 5B). Notably, the negative correlation between cell length and cell speed, consistent with the stick-slip regime, was confirmed for most of cell lines.

Our findings demonstrate that a stochastic stick-slip mechanism, which is intrinsically based on the properties of adhesion dynamics, is a very robust feature of adherent cell migration. In particular, while this mechanism provides a simple scenario of spontaneous symmetry breaking and cell polarization, our results do not exclude that stick-slip behavior might also occur in the presence of other polarization mechanisms.

Conclusion

To summarize, we presented an original 1D migration assay based on a combination of soft micropatterning, force imaging, and optogenetics. Movement of cells was restricted along thin adhesive lines and characterized by a distinctive spatiotemporal force pattern. Because of this, we were able to extract and interpret migratory and force parameters in a simplified and straightforward manner, while, at the same time, partially mimicking relevant physiological conditions of 3D fibrillar migration absent in conventionally performed 2D migration studies (*26*).

Applying this 1D approach in combination with a theoretical framework, we have uncovered a generic stick-slip mechanism, which complements previous studies. Other studies have proposed distinct symmetry breaking scenarios, which emerge either within the front or rear of a cell, generating a cytoskeletal polarity (and hence force asymmetry) before the initiation of migration (*20*, *21*). In contrast, our proposed mechanism allows cells to spontaneously break their symmetry by stochastically detaching adhesive contacts on one side, resulting in a migratory step in the opposite direction. The main originality of our work is that symmetry breaking can emerge independently of a prior polarity of the actin cytoskeleton, due to instabilities of the mechanochemical coupling of the cell to its environment via adhesion sites. This process is controlled by the interplay of contractile forces and focal adhesion dynamics. Hence, by modifying contractility and adhesiveness of the cell, the rate of such stochastic steps (i.e., the instantaneous speed of cell motion) can be controlled. Although the focus of this paper is on mesenchymal cell migration, we anticipate that amoeboid motility could be understood as an extreme regime of a similar mechanism, in which a high adhesion turnover rate causes cells to remain within a fast-moving slip phase. In addition, we found that stochastic stick-slip is responsible for a negative correlation between cell length and cell speed, which we observed across many cell types, thereby suggesting the relevance and robustness of this mechanism beyond the specific 1D assay and the two main cell types that we analyzed in this paper. In light of our findings, cell length represents a direct readout of cell adhesiveness and thus appears as a straightforward parameter to predict cell migratory behavior.

Our stick-slip model explains the adhesion-dependent initiation of migration with an equal probability for cells to start moving in either one of the two possible directions. Yet, once symmetry was broken, we observed cells exhibiting either oscillatory motion with frequent directional changes or persistent movement in one direction. However, how the first stochastic step can lead to the emergence of persistent migration remains out of the scope of our study. Other

mechanisms regulating polarity are likely to be at play after initiation of migration and are expected to bias the direction of movement and/or reinforce persistence once symmetry is broken [e.g., other force-generating cytoskeleton systems like the microtubule network as well as the positioning of its organizing center the centrosome (*45*, *46*)]. Together, stochastic stick-slip appears as a basic mechanism of symmetry breaking for various adherent mammalian cell types, which can coexist with other polarization mechanisms.

MATERIALS AND METHODS

Experimental design

The general goal of this study was to unravel a temporal sequence of events by following the evolution of the mechanical cell-substrate interaction during spontaneous symmetry breaking. To do so, we designed an in vitro cell migration assay. Our in vitro approach allowed us to simultaneously extract morphometric and mechanical parameters. To do so, our experimental setup was based on a combination of different techniques: The migration assay that we developed is based on microfabrication of thin adhesive linear tracks on soft substrates and force imaging. This bottom-up approach was used to identify key regulating mechanical parameters during spontaneous symmetry breaking. In addition, we further validated and challenged our findings by using pharmacological treatments and optogenetic approaches and extended our study by screening various cell types.

Cell culture

RPE1 wild type (WT) (provided by L. Blanchoin, Cytomorpholab Grenoble, France and stably transfected with vinculin-eGFP by Y. A. Miroshnikova, Institute of Advanced Biology, France), NIH-3T3 WT (gift by H. Maiato, University of Porto, Portugal and stably transfected with vinculin-eGFP by Y. A. Miroshnikova, Institute of Advanced Biology, France), and NIH-3T3 optoGEF_RhoA (given by M. Coppey, Institute Curie, France) were cultured under standard cell culture conditions (37°C, 5% CO_2) in Gibco Dulbecco's Modified Eagle Medium/Nutrient Mixture F-12 (DMEM)/F-12 GlutaMAX and Gibco DMEM GlutaMAX (Life Technologies), respectively, containing 10% heat-inactivated fetal bovine serum (Life Technologies) and penicillin/streptomycin (100 μg/ml) (Sigma-Aldrich).

Cells were plated on patterned polyacrylamide (PAA) hydrogels at a low density of 6×10^3 cm^{-2} and allowed to spread for 2 to 4 hours. For life imaging, the medium of NIH-3T3 WT/vin-eGFP/optoGEF_RhoA was replaced by Leibovitz's L-15 medium (Life Technologies).

Soft micropatterning

Fibronectin line patterned PAA hydrogels were microfabricated using the glass technique described by Vignaud *et al.* (*47*). In short, 32-mm glass coverslips (VWR) were plasma-treated for 30 s and incubated for 30 min at room temperature (RT) with poly-L-lysine–grafted–polyethylene glycol (0.1 mg/ml, pLL-PEG, SuSoS) diluted in Hepes [10 mM (pH 7.4), Sigma-Aldrich). After washing in deionized phosphate-buffered saline (dPBS, Life Technologies), the pLL-PEG–covered coverslip was placed with the polymer brush facing downward onto the chrome side of a quartz photomask (Toppan) for photolithography treatment (5-min ultraviolet-light exposure, UVO Cleaner Jelight). Subsequently, the coverslip was removed from the mask and coated with fibronectin (20 μl/ml) (Sigma-Aldrich) and Alexa Fluor 546–conjugated fibrinogen (20 μl/ml) (Invitrogen) diluted in dPBS for 30 min at RT. In the meantime, a premix of acrylamide (Sigma-Aldrich), *N*,*N*-methylenebis (acrylamide) (Sigma-Aldrich) and dPBS was mixed [ratio for a final Young modulus of 40 kPa described in (*48*)] and degased for 20 min. After, fluorescent nanobeads (dark red, F-8807 PS Invitrogen; dragon green, FCDG003 Bangs Laboratories) were added to the premix, and the dispersion was sonicated for 5 min (Bandelin Sonorex). To initiate polymerization, 1 μl of ammonium persulfate and 1 μl of tetramethylethylenediamine were added to 165 μl of premix and vortexed. A drop of 47 μl was immediately placed onto the protein-coated glass coverslip and covered with a previously silanized glass coverslip. Salinization was facilitated beforehand by treating the glass surface with 100% ethanol (Fluka Analytical) containing 0.0035% (v/v) PlusOne Bind-Silane (GE Healthcare Life Science) and 0.0035% (v/v) acetic acid (Sigma-Aldrich). After 30 min of polymerization at RT, the sandwiched coverslips were emerged in double-distilled water (ddH_2O) and separated with a scalpel. The PAA hydrogel patterned with fibronectin attached to the silanized coverslip and was stored in dPBS at 4°C for up to 1 week.

Drug treatment

After at least 3 hours of cell spreading, either one of the following inhibitors was added: 3 μM blebbistatin (Sigma-Aldrich) or 1 μM pF573,288 (Sigma-Aldrich). Control samples were treated with 0.025% dimethyl sulfoxide (Sigma-Aldrich).

For static imaging, cells were fixed after two subsequent hours of incubation with the inhibitor. For live imaging, cells were exposed to the inhibitor for up to 16 hours.

Before permeabilization and fixation

RPE1 vin-eGFP and NIH-3T3 vin-eGFP cells were fixed after 5 hours of spreading. First, cells were prepermeabilized using 0.25% Triton X-100 (Sigma-Aldrich) diluted in cytoskeleton buffer [10 mM 2-ethanesulfonic acid (MES, Sigma-Aldrich), 100 mM potassium chloride (KCl, Sigma-Aldrich), and 3.6 mM magnesium chloride hexahydrate ($MgCl\ 6H_2O$, Sigma-Aldrich), and 1.9 mM aminopolycarboxylic acid (EGTA, Sigma-Aldrich) in ddH_2O]. The sample was quickly rinsed with the prepolymerization solution and immediately placed into the fixation buffer [4% paraformaldehyde and 10% (w/v) sucrose (Sigma-Aldrich) in cytoskeleton buffer]. After 15-min fixation at RT, samples were washed once with cytoskeleton buffer and blocked for 30 min at RT with blocking buffer [0.5% bovine serum albumin (Sigma-Aldrich), 0.1% sodium azide (NaN_3, Sigma-Aldrich), and 20 mM glycine (Sigma-Aldrich) in dPBS]. For additional staining of filamentous actin (F-actin), samples could be incubated for 30 min at RT with Alexa Fluor 647 phalloidin (Sigma-Aldrich) diluted in blocking buffer (1:1000). The fixed sample was mounted onto a glass slide using Fluoromount-G (Electron Microscopy Sciences) and stored at 4°C.

Adhesion imaging and analysis

Static adhesion imaging was performed on fixed samples using an inverted confocal microscope (Leica TCS-SP8) using a 40× objective (oil immersion, numerical aperture 1.3). Individual adhesion sizes of different conditions were extracted with Fiji using an approach described previously (*49*).

For dynamic adhesion imaging, NIH-3T3 vin-eGFP, RPE1 vin-eGFP, or NIH-3T3 optoGEF_RhoA cells were plated on fibronectin line patterned glass substrates to enable TIRFm. We used an inverted microscope (Axiovert 200 M, Zeiss) equipped with a charge-coupled

device (CCD) camera (Clara CCD, Andor) and a 488-nm argon laser. Cells were kept at 37°C and imaged every minute for at least 1 hour. Adhesion dynamics were quantitatively analyzed plotting a kymograph using Fiji. Blue light–induced adhesion modification was quantified by measuring the vinculin-iRFP recruitment within the photoactivation area. To do so, the integrated fluorescence intensity was measured per image frame using Fiji.

FRAP experiments were performed on NIH-3T3 vin-eGFP and RPE1 vin-eGFP plated on patterned 40-kPa hydrogels using an inverted confocal spinning disk microscope (Andromeda, TILL-FEI). Each FRAP experiment was performed as follows: prebleach, bleach, and recovery. Images were acquired every 500 ms. First, the signal was monitored over 50 time points before photobleaching (prebleach). Per cell, two adhesive cluster located at the edge of the cell were bleached within two rectangular regions of interest (ROIs) of 7.5 μm^2 using a 488-nm laser at full power (bleach). Afterward, we followed the fluorescence signal over 100 time points (recovery). After waiting for 5 min, the experiment was repeated twice for the same ROIs within the same cell. The extracted fluorescence signal was fit with a biexponential curve to extract a slow and fast component ratio equivalent to the free vinculin within the cytosol and the vinculin engaged within adhesions, respectively.

Traction force microscopy

Experimentally, force measurements were conducted on cells after 2 to 4 hours of spreading using an inverted microscope (Nikon T*i*-E) with a Zyla sCMOS camera (Andor) and a temperature control system set at 37°C. Single-cell force measurements were performed using a method described previously (*25*). Images of fluorescent beads within the stressed and relaxed polyacrylamide substrate were taken before and after detachment of the adherent cell, respectively. The displacement field analysis was done using a homemade algorithm based on the combination of particle image velocimetry and single-particle tracking. After drift correction, bead images were divided into smaller subimages (9.22 μm). Cross-correlating corresponding subimages in the stressed and reference images yields the mean displacement over each considered region. After correcting this mean displacement, single-particle tracking was performed in each subimage, leading to displacement measurements of high accuracy and a spatial resolution of 20 nm. The final displacement field was interpolated on a regular grid with 1.15-μm spacing. From that, cellular traction forces were computed using Fourier transform traction cytometry with zero-order regularization (*28*, *50*), under the assumption that the substrate is a linear elastic half-space and considering only in-plane displacement and stress (tangential to the substrate). The final traction stress was obtained on a grid with 1.15-μm spacing. To estimate the total force exerted by a cell, local stress values multiplied by the unit grid area are summed over the whole cell area. All calculations and image processing were performed with MATLAB.

1D dipole and quadrupole analysis

Cells on lines are analyzed in 1D by projecting and summing all cell-exerted traction on the axis of the line. Typically, the 1D traction exhibit two peaks, one at each cell edge, that are respectively oriented toward the positive and negative directions, forming a contractile dipole. First, small stress values corresponding to noise (less than 10% of the stress peak value) were filtered out. Then, positive- and negative-oriented tractions were considered separately. The first order moment of each traction peak was used to derive the center of mass for each traction peak: $x_s = (\int x T_s dx)/(\int T_s dx)$, where the sign s is either positive or negative referring to the considered traction direction. Then, the width of each stress peak was evaluated by computing its second-order moment centered on each center of mass, x_s, by: $D_s = \int (x - x_s)^2 T_s dx/(\int T_s dx)$. Last, the asymmetry factor is obtained from the normalized difference between the width of positive- and negative-oriented traction, $(D_+ - D_-)/(D_+ + D_-)$. This factor is closely related to the "force quadrupole" used in other works. It has values between −1 and 1. Its amplitude quantifies the degree of force asymmetry (0 corresponding to a symmetric stress distribution), and its sign indicates the direction of this asymmetry.

In this way, the force asymmetry is evaluated at each time point (one point every minute) on TFM movies of cells on lines. To statistically investigate the force-motion relation, we divided the 4- to 5-hour movies into 30-min intervals. For each time interval, the cell was deemed to be either in a static or a moving phase based on the average velocity of its nucleus. Static phases correspond to velocity slower than 0.1 μm/min, while moving phases correspond to velocity higher than 0.3 μm/min. The mean asymmetry amplitude was calculated by averaging the force asymmetry factor over each 30-min interval. Since cells motion have equal probability to be directed toward the right or the left, raw asymmetry values are centered around zero. To distinguish noise from motion-induced asymmetry, the final asymmetry amplitude was defined as the raw asymmetry values multiplied by the sign of the cell velocity (averaged over the same interval).

F-actin staining and asymmetry analysis

Silicon rhodamine (SiR)–actin (Spirochrome) was used to stain F-actin within life cells. Cells were incubated overnight with 100 nM SiR-actin and 10 μM verapamil. A Nikon T*i*-E inverted microscope was used to image the cytoskeleton structure over several hours.

Actin fluorescence images were analyzed to quantify actin asymmetry using the following procedure: After smoothing, the image was divided at the position of the cell nucleus into two subimages, corresponding to the left and right edges of the cell. The transverse actin distribution width each extremity, W_{left} and W_{right}, were estimated by projecting each subimage onto a line orthogonal to the migration axis and by calculating the centered second-order moment of the resulting profile. Comparing these two widths enabled us to quantify asymmetries in the shape of the actin distribution. The asymmetry factor was defined as: $\frac{W_{right} - W_{left}}{W_{right} + W_{left.}}$

Optogenetic experiments

Our Nikon T*i*-E inverted, fluorescent microscope was equipped with a digital mirror device (Nikon) to locally control area of illumination with a 460-nm light-emitting diode. NIH-3T3 optoGEF_RhoA cells were plated as described on patterned hydrogels and kept at 37°C during all optogenetic experiments. Images were acquired every 15 or 60 s. First, cells were observed before photostimulation for at least 10 min. During the subsequent photoactivation cycle, one side of the cell was locally exposed to 150-ms blue-light pulses every minute over a period of at least 15 min. A relaxation period of at least 15 min was done in between two subsequent photoactivation cycles. We were able to perform bead imaging for TFM and/or actin imaging in parallel with the optogenetic stimulation.

Position tracking and cell length/velocity measurements

Single-cell tracking and extraction of morphometric parameters (front, rear, and nucleus positions) was performed on time-lapse bright-field images of cells migrating on lines by manually clicking on those structures on each frame. Images acquired in the present work (RPE and NIH cells) have been recorded every 5 min, while data originating from the cell race have an interval of 15 min between frames.

The time traces of the morphometric parameters were analyzed in MATLAB. First, the cell center position (middle of the front and rear positions) was smoothed by convolution with a 15-min flat window. The migration velocity and cell length were calculated over an interval of 30 min. We chose this short interval to capture the instantaneous velocity (knowing that the cell race videos have a temporal resolution of 15 min). Then, these instantaneous velocities (in absolute value) and the cell length were averaged over one time trace corresponding to one cell. Each cell was represented by one data point in the velocity versus length graph depicting different cell types. Videos of PRE1 and NIH-3T3 (with or without inhibitor) had a higher time resolution (one frame every 5 min) but were smoothed, and migration parameters were calculated over the same time interval used for the cell race data.

Statistical analysis

All data were plotted and statistically analyzed in GraphPad Prism (GraphPad Software, San Diego, CA, USA). To test the significance in between data, we performed two-tailed Student's *t* tests. Error bars on graphs represent the SD. If a linear fit was applied, GraphPad Prism computed it with a confidence interval of 95%.

SUPPLEMENTARY MATERIALS

Supplementary material for this article is available at http://advances.sciencemag.org/cgi/content/full/6/1/eaau5670/DC1

Supplementary Text

Fig. S1. Polarization of the actin cytoskeleton.

Fig. S2. Mechanical interaction between the cell and its environment decreases upon the initiation of migration.

Fig. S3. Force-length correlation during stick-slip migration.

Movie S1. Adhesion dynamics of RPE1 and NIH-3T3 cells.

REFERENCES AND NOTES

1. J. Renkawitz, M. Sixt, Mechanisms of force generation and force transmission during interstitial leukocyte migration. *EMBO Rep.* **11**, 744–750 (2010).
2. D. J. Webb, J. T. Parsons, A. F. Horwitz, Adhesion assembly, disassembly and turnover in migrating cells–over and over and over again. *Nat. Cell Biol.* **4**, E97–E100 (2002).
3. A. J. Ridley, M. A. Schwartz, K. Burridge, R. A. Firtel, M. H. Ginsberg, G. Borisy, J. T. Parsons, A. R. Horwitz, Cell migration: Integrating signals from front to back. *Science* **302**, 1704–1709 (2003).
4. P. Friedl, K. Wolf, Plasticity of cell migration: A multiscale tuning model. *J. Cell Biol.* **188**, 11–19 (2009).
5. P. Monzo, Y. K. Chong, C. Guetta-Terrier, A. Krishnasamy, S. R. Sathe, E. K. F. Yim, W. H. Ng, B. T. Ang, C. Tang, B. Ladoux, N. C. Gauthier, M. P. Sheetz, Mechanical confinement triggers glioma linear migration dependent on formin FHOD3. *Mol. Biol. Cell* **27**, 1246–1261 (2016).
6. F. van Zijl, G. Krupitza, W. Mikulits, Initial steps of metastasis: Cell invasion and endothelial transmigration. *Mutat. Res.* **728**, 23–34 (2011).
7. A. Huttenlocher, A. R. Horwitz, Integrins in cell migration. *Cold Spring Harb. Perspect. Biol.* **3**, a005074 (2011).
8. O. T. Fackler, R. Grosse, Cell motility through plasma membrane blebbing. *J. Cell Biol.* **181**, 879–884 (2008).
9. A. J. Lomakin, K.-C. Lee, S. J. Han, D. A. Bui, M. Davidson, A. Mogilner, G. Danuser, Competition for actin between two distinct F-actin networks defines a bistable switch for cell polarization. *Nat. Cell Biol.* **17**, 1435 (2015).
10. D. A. Lauffenburger, A. F. Horwitz, Cell migration: A physically integrated molecular process. *Cell* **84**, 359–369 (1996).
11. Y. H. Tee, T. Shemesh, V. Thiagarajan, R. F. Hariadi, K. L. Anderson, C. Page, N. Volkmann, D. Hanein, S. Sivaramakrishnan, M. M. Kozlov, A. D. Bershadsky, Cellular chirality arising from the self-organization of the actin cytoskeleton. *Nat. Cell Biol.* **17**, 445–457 (2015).
12. A. M. Turing, The chemical basis of morphogenesis. *Philos. Trans. R. Soc., B* **237**, 37–72 (1952).
13. A. C. Callan-Jones, J.-F. Joanny, J. Prost, Viscous-fingering-like instability of cell fragments. *Phys. Rev. Lett.* **100**, 258106 (2008).
14. C. Blanch-Mercader, J. Casademunt, Spontaneous motility of actin lamellar fragments. *Phys. Rev. Lett.* **110**, 078102 (2013).
15. R. J. Hawkins, M. Piel, G. Faure-Andre, A. M. Lennon-Dumenil, J. F. Joanny, J. Prost, R. Voituriez, Pushing off the walls: A mechanism of cell motility in confinement. *Phys. Rev. Lett.* **102**, 058103 (2009).
16. A. C. Callan-Jones, R. Voituriez, Actin gel model of amoeboid cell motility. *New J. Phys.* **15**, 025022 (2013).
17. V. Ruprecht, S. Wieser, A. Callan-Jones, M. Smutny, H. Morita, K. Sako, V. Barone, M. Ritsch-Marte, M. Sixt, R. Voituriez, C.-P. Heisenberg, Cortical contractility triggers a stochastic switch to fast amoeboid cell motility. *Cell* **160**, 673–685 (2015).
18. L. P. Cramer, Forming the cell rear first: Breaking cell symmetry to trigger directed cell migration. *Nat. Cell Biol.* **12**, 628–632 (2010).
19. T. D. Pollard, G. G. Borisy, Cellular motility driven by assembly and disassembly of actin filaments. *Cell* **112**, 453–465 (2003).
20. S. Munevar, Y.-l. Wang, M. Dembo, Traction force microscopy of migrating normal and H-ras transformed 3T3 fibroblasts. *Biophys. J.* **80**, 1744–1757 (2001).
21. P. T. Yam, C. A. Wilson, L. Ji, B. Hebert, E. L. Barnhart, N. A. Dye, P. W. Wiseman, G. Danuser, J. A. Theriot, Actin–myosin network reorganization breaks symmetry at the cell rear to spontaneously initiate polarized cell motility. *J. Cell Biol.* **178**, 1207–1221 (2007).
22. J. P. Butler, I. M. Tolić-Nørrelykke, B. Fabry, J. J. Fredberg, Traction fields, moments, and strain energy that cells exert on their surroundings. *Am. J. Physiol.: Cell Physiol.* **282**, C595–C605 (2002).
23. M. Dembo, Y.-L. Wang, Stresses at the cell-to-substrate interface during locomotion of fibroblasts. *Biophys. J.* **76**, 2307–2316 (1999).
24. J. Lafaurie-Janvore, P. Maiuri, I. Wang, M. Pinot, J.-B. Manneville1, T. Betz, M. Balland, M. Piel, ESCRT-III assembly and cytokinetic abscission are induced by tension release in the intercellular bridge. *Science* **339**, 1625–1629 (2013).
25. Q. Tseng, I. Wang, E. Duchemin-Pelletier, A. Azioune, N. Carpi, J. Gao, O. Filhol, M. Piel, M. Théry, M. Balland, A new micropatterning method of soft substrates reveals that different tumorigenic signals can promote or reduce cell contraction levels. *Lab Chip* **11**, 2231–2240 (2011).
26. A. D. Doyle, F. W. Wang, K. Matsumoto, K. M. Yamada, One-dimensional topography underlies three-dimensional fibrillar cell migration. *J. Cell Biol.* **184**, 481–490 (2009).
27. S. L. Schuster, F. J. Segerer, F. A. Gegenfurtner, K. Kick, C. Schreiber, M. Albert, A. M. Vollmar, J. O. Rädler, S. Zahler, Contractility as a global regulator of cellular morphology, velocity, and directionality in low-adhesive fibrillary micro-environments. *Biomaterials* **102**, 137–147 (2016).
28. K. Mandal, I. Wang, E. Vitiello, L. A. Chacòn Orellana, M. Balland, Cell dipole behaviour revealed by ECM sub-cellular geometry. *Nat. Commun.* **5**, 5749 (2014).
29. A. Stéphanou, S. Le Floc'h, A. Chauvière, A hybrid model to test the importance of mechanical cues driving cell migration in angiogenesis. *Math. Model. Nat. Phenom.* **10**, 142–166 (2015).
30. M. Bergert, A. Erzberger, R. A. Desai, I. M. Aspalter, A. C. Oates, G. Charras, G. Salbreux, E. K. Paluch, Force transmission during adhesion-independent migration. *Nat. Cell Biol.* **17**, 524–529 (2015).
31. T. J. Mitchison, L. P. Cramer, Actin-based cell motility and cell locomotion. *Cell* **84**, 371–379 (1996).
32. B. Ladoux, R.-M. Mège, X. Trepat, Front–rear polarization by mechanical cues: From single cells to tissues. *Trends Cell Biol.* **26**, 420–433 (2016).
33. H. Wu, M. Thiébaud, W.-F. Hu, A. Farutin, S. Rafaï, M.-C. Lai, P. Peyla, C. Misbah, Amoeboid motion in confined geometry. *Phys. Rev. E* **92**, 050701 (2015).
34. L. B. Smilenov, A. Mikhailov, R. J. Pelham Jr., E. E. Marcantonio, G. G. Gundersen, Focal adhesion motility revealed in stationary fibroblasts. *Science* **286**, 1172–1174 (1999).
35. K. Kruse, J. F. Joanny, F. Jülicher, J. Prost, K. Sekimoto, Generic theory of active polar gels: A paradigm for cytoskeletal dynamics. *Eur. Phys. J. E Soft Matter* **16**, 5–16 (2005).
36. L. Valon, F. Etoc, A. Remorino, F. di Pietro, X. Morin, M. Dahan, M. Coppey, Predictive spatiotemporal manipulation of signaling perturbations using optogenetics. *Biophys. J.* **109**, 1785–1797 (2015).
37. C. G. Galbraith, K. M. Yamada, M. P. Sheetz, The relationship between force and focal complex development. *J. Cell Biol.* **159**, 695–705 (2002).
38. P. Maiuri, J.-F. Rupprecht, S. Wieser, V. Ruprecht, O. Bénichou, N. Carpi, M. Coppey, S. De Beco, N. Gov, C.-P. Heisenberg, C. L. Crespo, F. Lautenschlaeger, M. L. Berre, A.-M. Lennon-Dumenil, M. Raab, H.-R. Thiam, M. Piel, M. Sixt, R. Voituriez, Actin flows mediate a universal coupling between cell speed and cell persistence. *Cell* **161**, 374–386 (2015).

39. P. Maiuri, E. Terriac, P. Paul-Gilloteaux, T. Vignaud, K. McNally, J. Onuffer, K. Thorn, P. A. Nguyen, N. Georgoulia, D. Soong, A. Jayo, N. Beil, J. Beneke, J. C. H. Lim, C. P.-Y. Sim, Y.-S. Chu; WCR participants, A. Jiménez-Dalmaroni, J.-F. Joanny, J.-P. Thiery, H. Erfle, M. Parsons, T. J. Mitchison, W. A. Lim, A.-M. Lennon-Duménil, M. Piel, M. Théry, The first World Cell Race. *Curr. Biol.* **22**, R673–R675 (2012).
40. Z. Liu, P. Bun, N. Audugé, M. Coppey-Moisan, N. Borghi, Vinculin head–tail interaction defines multiple early mechanisms for cell substrate rigidity sensing. *Integr. Biol.* **8**, 693–703 (2016).
41. M. Kovács, J. Tóth, C. Hetényi, A. Málnási-Csizmadia, J. R. Seller, Mechanism of Blebbistatin inhibition of myosin II. *J. Biol. Chem.* **279**, 35557–35563 (2004).
42. J. K. Slack-Davis, K. H. Martin, R. W. Tilghman, M. Iwanicki, E. J. Ung, C. Autry, M. J. Luzzio, B. Cooper, J. C. Kath, W. G. Roberts, J. T. Parsons, Cellular characterization of a novel focal adhesion kinase inhibitor. *J. Biol. Chem.* **282**, 14845–14852 (2007).
43. J. Renkawitz, K. Schumann, M. Weber, T. Lämmermann, H. Pflicke, M. Piel, J. Polleux, J. P. Spatz, M. Sixt, Adaptive force transmission in amoeboid cell migration. *Nat. Cell Biol.* **11**, 1438–1443 (2009).
44. Y.-J. Liu, M. Le Berre, F. Lautenschlaeger, P. Maiuri, A. Callan-Jones, M. Heuzé, T. Takaki, R. Voituriez, M. Piel, Confinement and low adhesion induce fast amoeboid migration of slow mesenchymal cells. *Cell* **160**, 659–672 (2015).
45. J. Zhang, W.-H. Guo, Y.-L. Wang, Microtubules stabilize cell polarity by localizing rear signals. *Proc. Natl. Acad. Sci. U.S.A.* **111**, 16383–16388 (2014).
46. S. Etienne-Manneville, A. Hall, Integrin-mediated activation of Cdc42 controls cell polarity in migrating astrocytes through PKCζ. *Cell* **106**, 489–498 (2001).
47. T. Vignaud, H. Ennomani, M. Théry, Polyacrylamide hydrogel micropatterning. *Methods Cell Biol.* **120**, 93–116 (2014).
48. J. R. Tse, A. J. Engler, Preparation of hydrogel substrates with tunable mechanical properties. *Curr. Protoc. Cell Biol.* **Chapter 10**, Unit 10.16 (2010).
49. U. Horzum, B. Ozdil, D. Pesen-Okvur, Step-by-step quantitative analysis of focal adhesions. *MethodsX* **1**, 56–59 (2014).
50. B. Sabass, M. L. Gardel, C. M. Waterman, U. S. Schwarz, High resolution traction force microscopy based on experimental and computational advances. *Biophys. J.* **94**, 207–220 (2008).

Acknowledgments: We thank M. Piel and P. Maiuri for valuable discussions and sharing the cell race data with us. We also thank T. Boudou and M. Théry for critical discussions, J. Bernard for technical assistance, and members of the MOTIV team at LiPhy for support. We thank L. Blanchoin's Cytomorpholab in Grenoble for providing us RPE1 cells and H. Maiato from the University of Porto for providing us with NIH-3T3 cells. Furthermore, we want to thank A. Kyumurkov at the Institute of Advanced Biology in Grenoble for assisting with adhesion imaging. **Funding:** This work was supported by Nanoscience Fondation (M.B.), the ARC Fondation (M.B.), and the grant ANR-17-CE30-0032-01 of the French Agence Nationale de la Recherche. This work has been partially supported by the LabeX Tec 21 (Investissements d'Avenir: grant agreement no. ANR-11-LABX-0030). **Author contributions:** K.H. performed experiments and analyzed the data. S.D. performed optogenetic experiments on vinculin-iRFP–transfected cells. L.V. designed the optogenetic cell line in M.C.'s laboratory. Y.A.M. designed the vinculin-eGFP RPE1 and NIH-3T3 cells in C.A.-R.'s laboratory. C.F. provided insights on the FRAP experiments and performed the related data analysis. R.V. developed the theoretical framework. M.B. supervised the research. All authors contributed to writing the paper. **Competing interests:** The authors declare that they have no competing interests. **Data and materials availability:** All data needed to evaluate the conclusions in the paper are present in the paper and/or the Supplementary Materials. Additional data related to this paper may be requested from the authors.

Submitted 23 June 2018
Accepted 29 October 2019
Published 3 January 2020
10.1126/sciadv.aau5670

Citation: K. Hennig, I. Wang, P. Moreau, L. Valon, S. DeBeco, M. Coppey, Y. A. Miroshnikova, C. Albiges-Rizo, C. Favard, R. Voituriez, M. Balland, Stick-slip dynamics of cell adhesion triggers spontaneous symmetry breaking and directional migration of mesenchymal cells on one-dimensional lines. *Sci. Adv.* **6**, eaau5670 (2020).

Science Advances

Stick-slip dynamics of cell adhesion triggers spontaneous symmetry breaking and directional migration of mesenchymal cells on one-dimensional lines

K. Hennig, I. Wang, P. Moreau, L. Valon, S. DeBeco, M. Coppey, Y. A. Miroshnikova, C. Albiges-Rizo, C. Favard, R. Voituriez and M. Balland

Sci Adv **6** (1), eaau5670.
DOI: 10.1126/sciadv.aau5670